

See discussions, stats, and author profiles for this publication at: <https://www.researchgate.net/publication/359680659>

High energy storage capacity, heterogeneous domain structure and stabilization of intermediate phase in PbZrO_3 -based antiferroelectric single crystals

Article in *Journal of Materials Chemistry C* · January 2022

DOI: 10.1039/D1TC05738C

CITATIONS

0

READS

77

8 authors, including:



Zenghui Liu

Xi'an Jiaotong University

45 PUBLICATIONS 243 CITATIONS

[SEE PROFILE](#)



Yi Yuan

Simon Fraser University

10 PUBLICATIONS 21 CITATIONS

[SEE PROFILE](#)



Zuo-Guang Ye

Simon Fraser University

588 PUBLICATIONS 18,489 CITATIONS

[SEE PROFILE](#)

Some of the authors of this publication are also working on these related projects:



Broadband inelastic light scattering spectroscopy of relaxor ferroelectrics [View project](#)



relaxor ferroelectric ceramics [View project](#)

Cite this: *J. Mater. Chem. C*, 2022, **10**, 6762

High energy storage capacity, heterogeneous domain structure and stabilization of intermediate phase in PbZrO₃-based antiferroelectric single crystals

Zenghui Liu,^a Zhixuan Guo,^a Hongyan Wan,^a Yi Yuan,^b Hao Yang,^a Hua Wu,^c Wei Ren^{*a} and Zuo-Guang Ye^{*b}

Lead zirconate PbZrO₃ (PZ)-based antiferroelectric (AFE) materials have received tremendous attention due to their potential applications in high density energy storage capacitors. However, PZ suffers from an ultrahigh critical electric field (E_F), making it unsuitable for practical applications. To develop new materials with better energy storage performances, a bismuth-based perovskite, Bi(Zn_{2/3}Nb_{1/3})O₃ (BZN) was introduced to PZ to form the PZ-BZN solid solution, and single crystals of this system were successfully grown from high temperature solution. The crystal structure, domain structure, and various physical properties of the crystals were investigated. The incorporation of BZN into PZ was found to stabilize the intermediate (IM) phase of rhombohedral symmetry existing between the AFE phase and the paraelectric (PE) phase. The origin of the IM phase was discussed. A heterogeneous ferroelastic/ferroelectric domain structure was found in the AFE phase of PZ-BZN, while a high domain wall density was observed in the IM phase. Most importantly, a significantly enhanced recoverable energy density was achieved together with improved dielectric permittivity and polarization in the PZ-BZN single crystals. This work unveils a novel single crystal material of high performance, potentially useful for energy storage applications, especially at mild temperatures, and provides a better understanding of the domain structure and the origin of the IM phase in PZ-based AFE materials, which will be beneficial to the design and synthesis of new AFE materials with better energy storage performances.

Received 30th November 2021,
Accepted 1st April 2022

DOI: 10.1039/d1tc05738c

rsc.li/materials-c

Introduction

Antiferroelectric (AFE) materials are of particular interest because of their unique properties, such as high energy storage density, large field-induced strain and giant electrocaloric effect, making them fundamental and indispensable functional materials for modern electronic devices and microelectromechanical systems (MEMS).^{1–5} AFE materials are characterized by the presence of sublattices with antiparallel dipolar alignments, giving rise to a zero net polarization and thereby the absence of ferroelectric (FE), pyroelectric and piezoelectric properties. However, under a sufficiently high electric field (larger than the critical electric field, E_F), the dipoles can be reoriented to align with the applied external electric field,

resulting in an electric field-induced AFE to FE phase transformation, which is characterized by double hysteresis loops of the polarization, P , as a function of the applied bipolar external electric field, E . Such a phase transformation is the physical basis for the numerous practical applications mentioned above.^{6–8}

To date, extensive investigations have been performed on lead zirconate PbZrO₃ (PZ)-based AFE materials from different perspectives.^{9–28} At room temperature, PZ shows AFE nature with the orthorhombic $Pbam$ space group. Upon heating, it undergoes a phase transformation from the AFE orthorhombic structure to a paraelectric (PE) cubic structure at around 235 °C.¹⁸ An intermediate (IM) ferroelectric phase was found to exist between the AFE and the PE phases in some PZ single crystals¹⁹ and ceramics.²⁰ Further investigation indicates that the IM phase arises from defects in the crystal lattice, such as Pb vacancies, oxygen vacancies or impurity atoms.^{15,21,29} However, how the defects influence the IM phase remains unclear.

From the practical point of view, pure PZ is not suitable for energy storage application due to its inherently high E_F at room temperature, which prevents the AFE to FE phase transition

^a Electronic Materials Research Laboratory, Key Laboratory of the Ministry of Education & International Center for Dielectric Research, Xi'an Jiaotong University, Xi'an 710049, China. E-mail: liu.z.h@xjtu.edu.cn, wren@xjtu.edu.cn

^b Department of Chemistry and 4D LABS, Simon Fraser University, Burnaby, British Columbia, V5A 1S6, Canada. E-mail: zye@sfu.ca

^c Department of Applied Physics, Donghua University, Ren Min Road 2999, Songjiang, Shanghai 201620, China

from happening. As a result, chemical modifications by doping or substitution with various cations, such as La^{3+} , Sn^{4+} , and Ti^{4+} , and by forming solid solutions, have been carried out to enhance the energy storage performance of PZ.^{22,23,30}

So far, most of the energy storage devices, for example, power pulse capacitors, have used antiferroelectric materials in the form of ceramics mostly due to their mechanical properties and cost effectiveness, and most of the research has also focused on AFE ceramics because of the difficulties encountered in growing single crystals.^{1–5,22,30} On the other hand, antiferroelectric single crystals usually exhibit better properties with higher dielectric permittivity, lower dielectric loss and larger polarization compared with their polycrystalline counterparts, making them promising candidates for energy storage applications, in particular, where high performance is required.^{31,32} In addition, from the fundamental research point of view, single crystals provide a unique platform to characterize their various anisotropic properties, such as ferroic domain structure, crystallographic dependence of the energy storage performance, *etc.*, which remain poorly understood.

Recently, special attention has been paid to bismuth-based perovskites in order to develop environment-friendly materials. Similar to lead, bismuth has the stereochemically active $6s^2$ lone pair electrons, which are helpful to induce large structural distortion so as to enhance polarization as in bismuth-based perovskites. Additionally, Bi^{3+} has a smaller ionic radius than that of Pb^{2+} ($r(\text{Bi}^{3+}) = 1.36 \text{ \AA}$ vs. $r(\text{Pb}^{2+}) = 1.49 \text{ \AA}$), which could lead to a bigger ionic displacement, inducing a larger polarization than that in lead-based counterparts. These features make bismuth-based perovskites a good modifier for designing new functional materials with desirable performances, such as ferroelectricity, piezoelectricity and antiferroelectricity.^{33–35}

In this work, a bismuth-based complex perovskite, $\text{Bi}(\text{Zn}_{2/3}\text{Nb}_{1/3})\text{O}_3$ (BZN), is used as a new modifier to improve the performances of PZ for application purposes. In particular, the resulting PZ-BZN solid solution is prepared in the form of single crystals by the flux method. The characterization results indicate that the critical field of PZ is reduced, and more importantly, the energy storage density is doubled by incorporating BZN into PZ at a mild temperature. The enhancement of properties is attributed to the unique heterogeneous ferroelastic domain structure in the PZ-BZN crystals. In addition, the origin of the IM phase induced in PZ-BZN is discussed.

Experimental procedures

Single crystals of PbZrO_3 and $0.9\text{PbZrO}_3\text{--}0.1\text{Bi}(\text{Zn}_{2/3}\text{Nb}_{1/3})\text{O}_3$ ($0.9\text{PZ--}0.1\text{BZN}$) were grown by the flux method. High purity PbO (99.9%), Bi_2O_3 (99.9%), ZrO_2 (99.9%), ZnO (99.9%) and Nb_2O_5 (99.9%) were weighed according to the stoichiometric compositions of PZ and $0.9\text{PZ--}0.1\text{BZN}$. Pb_3O_4 and B_2O_3 were used as composite flux with a molar ratio of $\text{Pb}_3\text{O}_4\text{:B}_2\text{O}_3 = 0.56\text{:}0.44$, and the solvent: flux ratio was $0.05\text{:}0.95$ for the growth of both crystals. In each growth process, the solute and flux were homogeneously mixed and loaded into a 100 ml

platinum crucible covered with a lid, which was then put into a crystal growth furnace. The mixture was heated from room temperature to $1100 \text{ }^\circ\text{C}$ at a heating rate of $5 \text{ }^\circ\text{C min}^{-1}$, dwelled for 12 h, and then slowly cooled down to $750 \text{ }^\circ\text{C}$ at a cooling rate of $2 \text{ }^\circ\text{C h}^{-1}$, followed by a faster cooling to room temperature in 8 h. The as-grown crystals were separated from the solidified flux by leaching in dilute hot nitric acid solutions.

The chemical compositions of the grown crystals were determined by X-ray fluorescence (XRF) spectrometry measurements (Bruker S8 Tiger). X-Ray diffraction (XRD) measurements were performed on powders obtained from ground crystals and on as-grown natural faces using an X-ray diffractometer (PANalytical Empyrean diffractometer with $\text{Cu K}_{\alpha 1}$ X-ray tube) at room temperature to determine the crystal structure and orientation. In addition, temperature-variable XRD was carried out from $30 \text{ }^\circ\text{C}$ to $230 \text{ }^\circ\text{C}$ using a Bruker D8 Advance diffractometer to study the structural phase transitions. Gold layers were deposited on the largest ($(001)_{\text{PC}}$, subscript "PC" stands for pseudocubic) crystal facets as electrodes for electric measurements. The dielectric permittivity and loss tangent were measured as a function of temperature at various frequencies using a Novocontrol broadband dielectric analyzer. The polarization-electric field, $P(E)$, hysteresis loops of the crystals were measured using a Radiant RT-66 standardized ferroelectric testing system.

For the optical domain structure investigations, crystals were mirror polished to less than $80 \text{ }\mu\text{m}$ thick parallel to the natural grown $(001)_{\text{PC}}$ faces. The crystal was heated and cooled several times between room temperature and $300 \text{ }^\circ\text{C}$ to eliminate the residual stress possibly induced by polishing. The domain structures of the PZ-BZN single crystal were examined by polarized light microscopy (PLM) using an Olympus BX60 microscope equipped with a heating/cooling stage (Linkam HTMS600E) and a digital camera. At each temperature, the PLM images were taken after the temperature was stabilized for 20 to 25 minutes.

Results and discussion

Crystal growth

The as-grown PZ and PZ-BZN single crystals have dimensions of 1 to 4 mm, and exhibit a cuboid morphology. The as-grown PZ single crystals are nearly transparent (see inset of Fig. 1(a)), indicating a good quality, while the PZ-BZN single crystals are yellowish (see inset of Fig. 1(b)), which is due to the formation of color-centres and related defects.

To determine the orientation of the crystals, selected PZ and PZ-BZN single crystals were polished parallel to the naturally grown faces. The X-ray diffraction patterns of the PZ and PZ-BZN crystal plates are shown in Fig. 1(a and b), respectively. Only the pseudocubic diffraction peaks of $\{h00\}$ ($h = 1, 2, 3, \dots$) are visible, which indicates that the naturally grown largest facets of the crystals are of $(100)_{\text{PC}}$ orientation.

From the X-ray fluorescence spectroscopic analysis, the chemical compositions of the as-grown PZ and PZ-BZN crystals were determined to be $\text{Pb}_{1.00}\text{Zr}_{1.00}\text{O}_{3.00}$ and $(\text{Pb}_{0.96}\text{Bi}_{0.01})_{\square_{0.03}}$

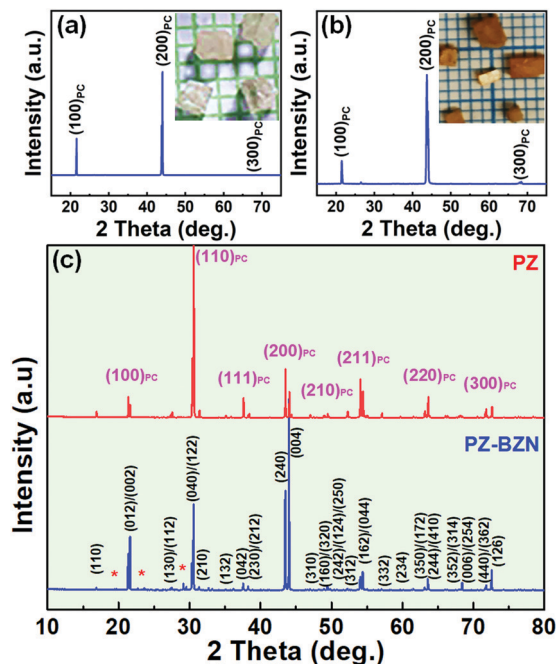


Fig. 1 (a and b) X-ray diffraction patterns of the naturally grown largest face of the PZ (a) and PZ-BZN (b) single crystals. The insets in (a and b) show the as-grown PZ and PZ-BZN single crystals, respectively. (c) XRD patterns of the PZ and PZ-BZN powders obtained from ground single crystals. The XRD patterns in (c) are indexed with both the pseudocubic setting (with subscript “PC”) and the orthorhombic setting. The impurity peaks are marked by stars (*).

($Zr_{0.95}Zn_{0.01}Nb_{0.04}(O_{2.97}\square_{0.03})$), respectively, with an overall accuracy better than ± 0.001 (where “ \square ” stands for vacancies). Thus, within the detection limit, the as-grown PZ crystal is considered to be stoichiometric. In contrast, the real composition of the grown PZ-BZN crystals differs significantly from the nominal composition of $(Pb_{0.9}Bi_{0.1})(Zr_{0.9}Zn_{0.07}Nb_{0.03})O_3$, suggesting a significant composition segregation which commonly occurs in the formation of solid solution crystals.^{36,37}

Crystal structure

The XRD patterns Fig. 1(c) shows the powder XRD patterns of the ground PZ and PZ-BZN single crystals at room temperature. The PZ crystals show a pure perovskite structure with an orthorhombic symmetry. The PZ-BZN crystals exhibit a similar pattern, indicating the same crystal structure as PZ (the impurity peaks marked by “*” in Fig. 1(c) likely arise from some inclusions in the ground crystals, which are absent in the XRD pattern of a clean as-grown crystal plate (Fig. 1(b)).

In order to determine the crystal structure, the diffraction patterns were fitted by the Pawley refinement method using TOPAS Academic software. The fitting was performed based on a model of *Pbam* space group, which is the commonly known symmetry for PZ at room temperature.^{9–17} The fitting results agree well with the selected model for both PZ and PZ-BZN (excluding the minor impurity peaks). Therefore, it can be concluded that both PZ and PZ-BZN crystallize in the orthorhombic *Pbam* space group. In comparison, PZ-BZN has smaller

Table 1 Calculated lattice parameters of the PZ and PZ-BZN single crystals at room temperature

Material system	Lattice parameters			Volume (\AA^3)
	<i>a</i> (\AA)	<i>b</i> (\AA)	<i>c</i> (\AA)	
PZ-BZN	5.87971 (4)	11.77705 (8)	8.22537 (3)	537.36
PZ	5.88395 (6)	11.78629 (12)	8.22781 (5)	570.60

lattice parameters than those of PZ, as shown in Table 1. The smaller lattice parameters result from the smaller average ionic radii of both A-site and B-site cations in BZN than in PZ [$r(\text{Bi}^{3+}) = 1.36 \text{ \AA}$, $r(\text{Zn}^{2+}) = 0.74 \text{ \AA}$, $r(\text{Nb}^{5+}) = 0.64 \text{ \AA}$, $r(\text{Pb}^{2+}) = 1.49 \text{ \AA}$, and $r(\text{Zr}^{4+}) = 0.72 \text{ \AA}$].³⁸

For the sake of clarity, the orthorhombic lattice setting of $\sqrt{2}a \times 2\sqrt{2}a \times 2a$ (where *a* represents the lattice dimension of the PE cubic phase) in PZ-based materials is commonly converted to the $a \times a \times a$ pseudocubic lattice setting by the following matrix:

$$(h_{\text{PC}}k_{\text{PC}}l_{\text{PC}}) = (hkl) \begin{pmatrix} 1/2 & -1/2 & 0 \\ 1/4 & 1/4 & 0 \\ 0 & 0 & 1/2 \end{pmatrix}, \quad (1)$$

where the subscript “PC” represents the pseudocubic setting. Under the pseudocubic setting, the $1/4(hkl)$ -type superlattice reflections are present in the powder diffraction patterns of PZ and PZ-BZN. The superlattice reflections arise from the antiparallel shifts of $\text{Pb}^{2+}/\text{Bi}^{3+}$ ions along the pseudocubic $\langle 110 \rangle$ direction, leading to the antiparallel polarizations and thereby the antiferroelectricity.^{9,39}

Dielectric properties and phase transitions

The temperature dependences of the dielectric permittivity (ϵ_r) and loss tangent of the $(001)_{\text{PC}}$ -oriented PZ and PZ-BZN single crystals were measured at various frequencies from 1 Hz to 1 MHz. Since no frequency dispersion of the dielectric maximum was observed, the variations of the dielectric permittivity and loss tangent measured at 100 kHz upon heating are selected and presented in Fig. 2 for clarity. The dielectric permittivity of the PZ and PZ-BZN single crystals peak at 230 °C and 222 °C, respectively, which corresponds to the respective Curie temperatures, T_C .

The temperature dependence of the dielectric permittivity of the PZ and crystal shows a sharp discontinuity at T_C , indicating a first-order transition from the AFE to PE phase. The PZ-BZN crystal also exhibits a sharp peak at T_C , and in addition, a shoulder is observed at T_{AF} just below T_C , as marked by an arrow in Fig. 2. This feature indicates the presence of an IM phase between the AFE and the PE phases, which is induced when BZN is incorporated into PZ, albeit at a small amount. A similar IM phase was previously found in some PZ and doped PZ crystals, and was reported to be ferroelectric.^{19,20}

As shown in the inset (1) of Fig. 2, in the PE phase (above T_C), the temperature dependences of $1/\epsilon_r$ for both the PZ and

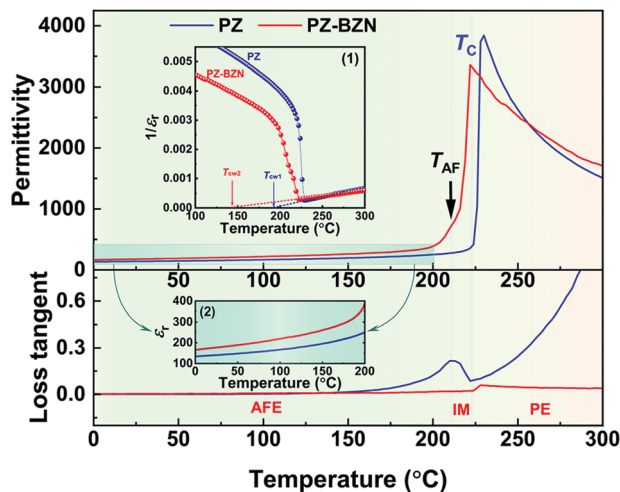


Fig. 2 Temperature dependences of the dielectric permittivity and loss tangent of (001)_{PC}-oriented PZ and PZ-BZN single crystals measured at 100 kHz upon heating. The inset (1) shows the temperature dependence of $1/\epsilon_r$, which exhibits a linear relation above T_C , following the Curie–Weiss law. The blue area in the dielectric permittivity curves is enlarged in inset (2).

PZ-BZN crystals fit well the Curie–Weiss law:

$$\frac{1}{\epsilon_r} = \frac{T - T_{CW}}{C}, \quad (2)$$

where ϵ_r is the dielectric permittivity, T the temperature, T_{CW} the Curie–Weiss temperature, and C the Curie constant. The Curie–Weiss temperature and the Curie constant were calculated to be $T_{CW} = 458$ K (185 °C) and 416 K (143 °C), and $C = 1.73 \times 10^5$ K and 2.65×10^5 K, for the PZ and PZ-BZN single crystals, respectively. The differences in these parameters are due to the different phase transition natures in the PZ and PZ-BZN crystals, which will be discussed in the subsequent sections.

The dielectric permittivity of the PZ-BZN crystal is larger than that of PZ at low temperatures. The rate of enhancement increases from 25% to 120% from 0 °C to 200 °C (see inset (2) of Fig. 2). The enhanced dielectric permittivity will lead to a larger polarization in PZ-BZN than that in PZ, which is favourable for better energy storage performance, as discussed in the following section. The loss tangent of both PZ and PZ-BZN is low ($<1\%$) in the temperature below 150 °C, above which the loss tangent of PZ-BZN increases rapidly and shows a peak at T_{AF} , in connection with the IM phase. Further increase of loss tangent at higher temperatures is due to the increase in the conductivity possibly induced by thermally activated defects.

Antiferroelectricity and energy storage performance

Fig. 3 shows the polarization (P) as a function of electric field (E) measured at 120 °C. At room temperature, an electric field up to 180 kV cm^{-1} (approaching the breakdown field) was not able to induce the AFE–FE phase transition. When heated up to 120 °C, both PZ and PZ-BZN single crystals exhibit typical double $P(E)$ hysteresis loops under ± 150 kV cm^{-1} at 10 Hz,

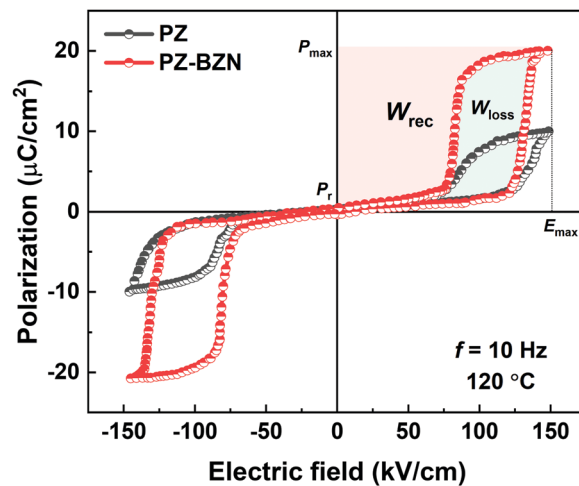


Fig. 3 Polarization - electric field double hysteresis loops of the PZ and PZ-BZN single crystals measured at 120 °C.

confirming the antiferroelectricity of the crystals at this temperature. The polarization induced in PZ-BZN under this condition is almost twice as large as that in the PZ single crystals. The E_F is determined as the average of the AFE-to-FE and FE-to-AFE transition fields, which decreases slightly from 113 kV cm^{-1} to 107 kV cm^{-1} in the PZ and PZ-BZN single crystals, respectively. The leakage current increases significantly when the crystals are further heated up, and this phenomenon becomes more prominent in the PZ-BZN single crystals.

The recoverable energy storage density (W_{rec}) equals to the area between the polarization axis and the FE-to-AFE switching hysteresis loop (the reddish-brown area in Fig. 3), which can be calculated by:

$$W_{\text{rec}} = \int_{P_r}^{P_{\text{max}}} E dP, \quad (3)$$

where P_r is the remnant polarization and P_{max} the maximum polarization. The energy loss density upon discharging equals to the area surrounded by the hysteresis loop (the green area in Fig. 3). From these parameters, the energy storage efficiency η can be calculated as:

$$\eta = \frac{W_{\text{rec}}}{W_{\text{rec}} + W_{\text{loss}}}. \quad (4)$$

The W_{rec} and η values calculated from the $P(E)$ hysteresis loops according to eqn (3) and (4) are 0.84 J cm^{-3} and 70.4%, and 1.6 J cm^{-3} and 63.7% in the PZ and PZ-BZN single crystals, respectively. The energy storage density achieved in PZ-BZN is larger than that of other AFE bulk materials, such as $(\text{Na}_{0.5}\text{Bi}_{0.5})\text{TiO}_3$ – SrTiO_3 , which are suitable for energy storage applications at elevated temperatures (120 °C).^{40,41} Compared with PZ, the significantly improved energy storage density in PZ-BZN results from the significantly enhanced induced polarization (P_{max}) and the unique domain structure in the PZ-BZN single crystals, which will be discussed in the subsequent section. Therefore, the PZ-BZN single crystals could be a

promising material potentially useful in energy storage applications, such as in pulsed power capacitors, especially at mild to high temperatures.

Heterogeneous ferroelastic/ferroelectric domain structure and evolution

The PLM technique, in conjunction with optical crystallography, allows direct observation and *in situ* analysis of the domain structures, phase symmetry, phase components and phase

transitions in single crystals, which are characteristic of ferroic materials. Detailed explanations on the principle of using PLM to determine the crystal symmetry of crystals can be found in ref. 34, 42. Fig. 4(a and b) show the PLM images of the optical domain structures of (001)_{PC}-oriented PZ and PZ-BZN single crystals at various temperatures, respectively.

At room temperature, the extinction of domains can be detected with the crossed polarizers at 45° to the [100]_{PC} edges for both crystals, as shown in Fig. 4(a1 and b1). When the

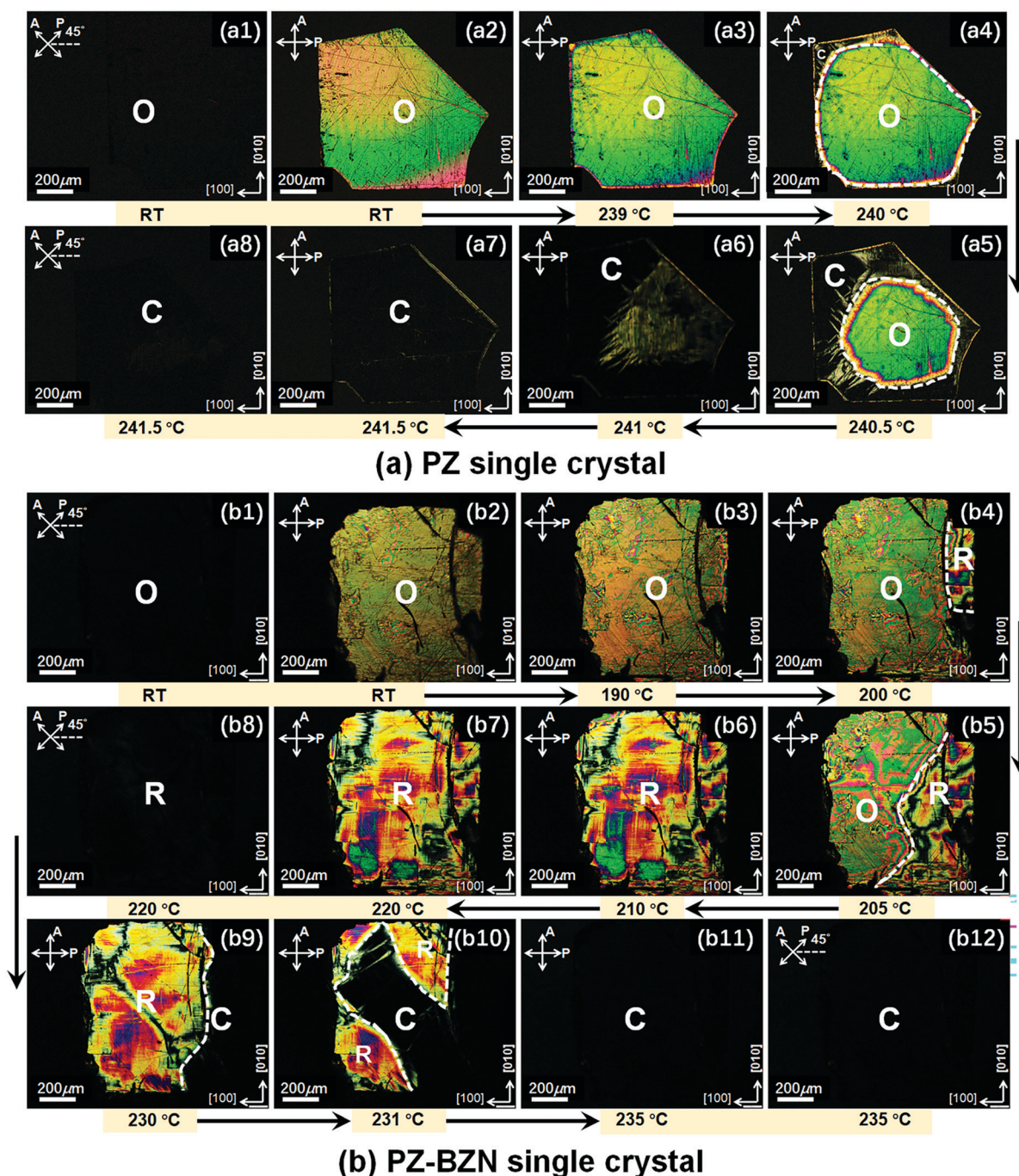


Fig. 4 Optical domain images of the (001)_{PC}-cut PZ (a) and PZ-BZN (b) single crystals under polarized light microscopy (PLM) with cross-polarizers at various temperatures (from room temperature to ~240 °C). O, R and C stand for orthorhombic, rhombohedral and cubic phases, respectively.

crossed polarizer and analyzer are parallel to the $[100]_{\text{PC}}$ edges of the crystal, the domains become birefringent. Such character is consistent with the orthorhombic symmetry of the crystals, in agreement with the XRD structural analysis. The PZ crystal shows an almost single ferroelastic domain state with uniform interference fringes (Fig. 4(a2)). In contrast, a multiple domain state appears in the PZ-BZN crystal with small domains embedded in large domain matrices (Fig. 4(b2)).

It is known that the domain switching kinetics is directly related to the domain structure.^{43–48} Due to the ferroelastic–ferroelectric domain interactions, the small ferroelastic domains can act as seeds, which then promote the polarization switching during the AFE-FE phase transition.^{44–47} Therefore, the heterogeneous ferroelastic domain structure appears in the PZ-BZN single crystal will decrease the E_{F} , lead to a larger induced polarization, and consequently enhance energy storage capacity when compared with PZ under the same electric field.

Upon heating, the colour of the interference patterns changes continuously in both crystals due to the gradual change of the birefringence. However, the ferroelastic domain structure remains almost unchanged until 239 °C (Fig. 4(a3)) and 190 °C (Fig. 4(b3)) in the PZ and PZ-BZN crystals, respectively.

When the temperature reaches 240 °C, the area at the edge of PZ crystal become extinct abruptly, indicating a direct phase transition from the low temperature AFE phase to the high temperature PE phase (Fig. 4(a4)). A slight increase of temperature leads to a movement of the phase boundary across the crystal (Fig. 4(a5)). A total optical extinction covers the whole crystal at 241.5 °C when the crystal completely transforms to the cubic phase (Fig. 4(a7 and a8)). A small bright area persists inconspicuously in-between 241 °C and 241.5 °C in part of the PZ crystal (Fig. 4(a6)), which might be related to a precursor effect as reported in ref. 49, 50. Therefore, no IM phase is observed between the AFE and PE phases, or if any, the temperature region of the IM phase would not exceed 0.5 °C.

It is a totally different scenario in the PZ-BZN single crystal thought. At ~190 °C, the domain structure begins to change dramatically, indicating a phase transformation from the low temperature orthorhombic AFE phase to an IM phase (which will be determined to be of rhombohedral symmetry). A clear domain boundary movement is observed upon heating (Fig. 4(b4 and b5)). Meanwhile, the size of the small domains of the orthorhombic phase grow rapidly, resulting in a labyrinth-like domain structure before the phase transition to the IM phase, as shown in Fig. 4(b5). After phase transition, the domain structure of the IM phase becomes stable and persists between ~210 °C and ~220 °C [Fig. 4(b6 and b7)]. In the IM phase, the extinction of domains can be found with the crossed polarizers at 45° to the $[100]_{\text{PC}}$ edges [Fig. 4(b8)]. With further increasing temperature, the crystal gradually transforms into a cubic phase with extinction at all angles between crossed polarizers above 235 °C (Fig. 4(b9 and b10)).

The domain structure of the PZ-BZN crystal at 220 °C (in the IM phase) is selected for further examination. As shown in Fig. 5(a), the domain structure reveals the coexistence of complex and different ferroelastic/ferroelectric domains.

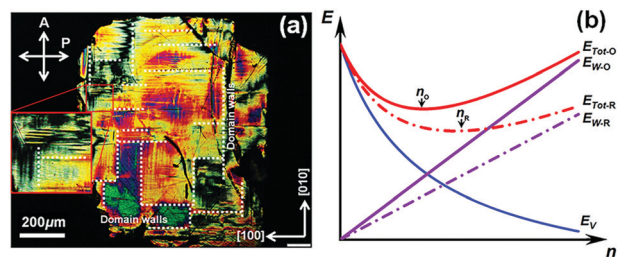


Fig. 5 (a) Domain structure of the $(001)_{\text{PC}}$ PZ-BZN single crystal observed under PLM at 220 °C. (b) Schematic diagram of the total energy (E_{Tot}) as a function of the number of domain walls (n). E_{V} mainly represents the elastic energy in the crystal. O and R in the subscripts stand for the orthorhombic and rhombohedral phases, respectively.

Stripe-like domains oriented along the $\langle 001 \rangle_{\text{PC}}$ directions appear with a width of 10–20 μm . In addition, the domain wall density increases remarkably in the IM phase compared to that in the AFE phase, which can be explained as follows. It is known that domains form in order to minimize the total energy (E_{Tot}), which can be written as,^{48,51,52}

$$E_{\text{Tot}} = E_{\text{V}} + E_{\text{W}}. \quad (5)$$

In this equation, E_{V} mainly represents the elastic energy in crystal, which decreases monotonically with the increase of the number of domains formed, and E_{W} refers to domain wall energy, which is proportional to the number of domain walls (n):

$$E_{\text{W}} = n \cdot S \cdot W, \quad (6)$$

where S is the area of the wall and W the domain wall energy density. As a result, the domain size and domain wall number are determined by the balance between E_{V} and E_{W} , so as to minimize the total energy. According to previous investigations,^{52,53} the domain wall energy density decreases with increasing temperature (or symmetry). In the PZ-BZN single crystals, the domain wall energy density in the rhombohedral (see the following section) intermediate phase ($E_{\text{W-R}}$) is lower than that in the orthorhombic phase ($E_{\text{W-O}}$). Therefore, more domain walls are formed to minimize the total energy, leading to a higher domain wall density. The variations of the total energy in the rhombohedral and orthorhombic phases and of the elastic energy as a function of domain wall density are schematically illustrated in Fig. 5(b).

Structural analysis of the IM phase

A notable feature of the PZ-BZN crystals is the appearance of an IM phase, which is not found in pure PZ single crystals grown under the same conditions. In order to clarify the crystal structure of the IM phase in the PZ-BZN single crystals, temperature-variable XRD measurements were carried out from 30 °C to 230 °C upon heating, as shown in Fig. 4. At 30 °C, the crystals have a typical orthorhombic symmetry, as evidenced by the presence of the $1/4(hkl)$ -type superlattice reflections marked by “♣”, the splitting of the pseudocubic $\{200\}_{\text{PC}}$ peak, and the appearance of a singlet $(111)_{\text{PC}}$ peak. Upon heating, the intensity of the superlattice peaks (in the blue dashed boxes in Fig. 6) gradually decreases before vanishing at around 200 °C, indicating

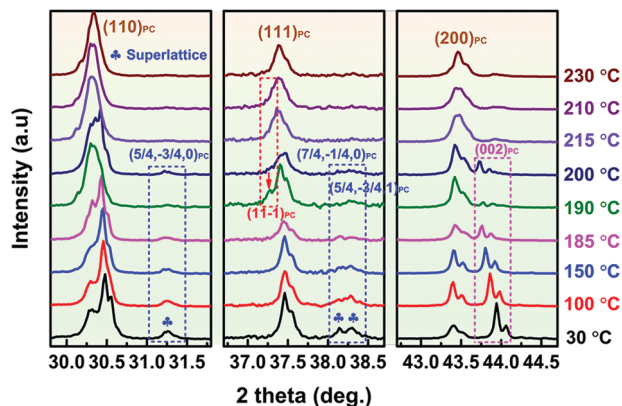


Fig. 6 XRD patterns of the ground PZ-BZN single crystals measured at various temperatures between 30 and 230 °C.

the phase transition from the orthorhombic phase to the IM phase. It should be noted that a shoulder develops at a lower angle of the $(111)_{\text{pc}}$ peak at temperatures higher than ~ 190 °C, which is indicative of a rhombohedral symmetry for the IM phase, while the $(5/4, -3/4, 0)_{\text{pc}}$, $(7/4, -1/4, 0)_{\text{pc}}$, $(5/4, -3/4, 1)_{\text{pc}}$ and $(002)_{\text{pc}}$ superlattice peaks remain unchanged until ~ 200 °C. Therefore, the rhombohedral and orthorhombic phases coexist between ~ 190 °C and ~ 200 °C. As the sample is further heated up, the $(111)_{\text{pc}}$ reflection peak gradually becomes a singlet at 230 °C, indicating that the crystal structure changes to the cubic symmetry. These results are consistent with the dielectric behavior and confirms the phase transition sequence from the orthorhombic AFE phase to the rhombohedral IM phase, and finally to the PE cubic phase upon heating.

The presence of the IM phase in the PZ-BZN single crystals, but not in the pure and stoichiometric PZ single crystals with high quality, suggests that the stabilization of the IM phase in PZ-BZN is due to the incorporation of the Bi^{3+} , Zn^{2+} and Nb^{5+} cations into the PZ lattice, which induces a considerable amount of defects. The existence of defects is expected to influence the type and dynamics of the soft modes and stabilize the IM phase in the PZ-BZN single crystals.^{10,54} According to the lattice dynamics theory, the paraelectric to antiferroelectric phase transition is intrinsically driven by the softening of a ferroelectric transverse optic polar mode at the Γ point of Brillouin zone. In the PZ-BZN single crystal, the softening of such mode leads to the stabilization of the IM phase below T_{C} . In contrast, in the stoichiometric PZ crystal, the IM phase is skipped due to the flexoelectric coupling effect.¹⁰ More detailed studies of PZ-BZN by total neutron scattering combined with theoretical modeling and calculations would be needed to clarify the mechanisms of these phase transitions.

Conclusions

To develop new dielectric materials for high density energy storage applications and to understand the crystal structure-property relations, antiferroelectric single crystals of PbZrO_3 and $\text{PbZrO}_3\text{-Bi}(\text{Zn}_{2/3}\text{Nb}_{1/3})\text{O}_3$ solid solution were grown by the

flux method. The crystal structure, domain structure, dielectric properties, phase transitions, and energy storage performance of the crystals were studied systematically. Both crystals show an orthorhombic symmetry at room temperature, characteristic of the AFE phase. The introduction of BZN into PZ stabilizes an intermediate phase in-between the AFE and PE phase, which is found to be of rhombohedral symmetry. By polarized light microscopy, small ferroelastic domains are revealed to be embedded in large domain matrix in the AFE phase of PZ-BZN crystal, showing an inhomogeneous domain structure, which differs from the homogeneous single ferroelastic domain state found in PZ. In the IM phase, the domain wall density increases significantly compared to that in the AFE phase. The stabilization of the IM phase in PZ-BZN single crystal is attributed to the defects which influence the local phonon modes. Most importantly, the introduction of BZN into PZ decreases the critical electric field so as to realize the AFE-FE phase transition, leading to a significant improvement in dielectric permittivity and polarization, and a doubled energy storage capacity compared to PZ single crystal at 120 °C. The enhancement of these physical properties is due to the beneficial effect of introducing bismuth-based perovskite and the unique heterogeneous ferroelastic domain structure formed in PZ-BZN, which promote the polarization switching coupled to the AFE-FE phase transition. This work has produced a promising single crystal material that is potentially useful as dielectric capacitors for high density energy storage application, especially at mild temperatures. On the fundamentals side, it also provides new insights into the domain structure and origin of the IM phase in PZ-based AFE materials, which in turn will help develop new AFE materials with better energy storage performances.

Conflicts of interest

There are no conflicts to declare.

Acknowledgements

The authors would like to thank Dr Guoqing Zhou at the Instrument Analysis Center of Xi'an Jiaotong University for his assistance with the XRF experiments. This work was supported by the Natural Science Foundation of China (Grant no. 51902244), the Fundamental Research Funds for the Central Universities of China (Grant no. xzy012021025), the China Postdoctoral Science Foundation (Grant no. 2018M643632), the Natural Science Foundation of Shaanxi Province of China (Grant No. 2019JQ-389), the "111 Project" of China (Grant no. B14040), the U.S. Office of Naval Research (Grant no. N00014-16-1-3106 and N00014-21-1-2085), and the Natural Sciences and Engineering Research Council of Canada (NSERC, Grant no. RGPIN-2017-06915).

References

- 1 C. A. Randall, Z. M. Fan, I. Reaney, L. Q. Chen and S. Trolier-McKinstry, *J. Am. Ceram. Soc.*, 2021, **104**, 3775–3810.

- 2 G. Wang, Z. Lu, Y. Li, L. Li, H. Ji, A. Feteira, D. Zhou, D. Wang, S. Zhang and I. M. Reaney, *Chem. Rev.*, 2021, **121**, 6124–6172.
- 3 X. Hao, J. Zhai, L. B. Kong and Z. Xu, *Prog. Mater. Sci.*, 2014, **63**, 1–57.
- 4 Z. Liu, T. Lu, J. Ye, G. Wang, X. Dong, R. Withers and Y. Liu, *Adv. Mater. Technol.*, 2018, **3**, 1800111.
- 5 L. T. Yang, X. Kong, F. Li, H. Hao, Z. X. Cheng, H. X. Liu, J. F. Li and S. J. Zhang, *Prog. Mater. Sci.*, 2019, **102**, 72–108.
- 6 C. Kittel, *Phys. Rev.*, 1951, **82**, 729.
- 7 W. Känzig, *Solid State Phys.*, 1957, **4**, 1–197.
- 8 P. Tolédano and M. Guennou, *Phys. Rev. B*, 2016, **94**, 014107.
- 9 E. Sawaguchi, H. Maniwa and S. Hoshino, *Phys. Rev.*, 1951, **83**, 1078.
- 10 A. Tagantsev, K. Vaideeswaran, S. Vakhrushev, A. Filimonov, R. Burkovsky, A. Shaganov, D. Andronikova, A. Rudskoy, A. Baron and H. Uchiyama, *Nat. Commun.*, 2013, **4**, 3229.
- 11 P. Tolédano and D. D. Khalyavin, *Phys. Rev. B*, 2019, **99**, 024105.
- 12 H. Liu, *J. Am. Ceram. Soc.*, 2018, **101**, 5281–5286.
- 13 M. Wu, D. S. Song, G. Vats, S. C. Ning, M. Y. Guo, D. W. Zhang, D. Q. Xue, S. J. Pennycook and X. J. Lou, *J. Mater. Chem. C*, 2018, **6**, 10332–10340.
- 14 Z. Fan, T. Ma, J. Wei, T. Yang, L. Zhou and X. Tan, *J. Mater. Sci.*, 2020, **55**, 4953–4961.
- 15 D. Kajewski, J. Kubacki, K. Balin, I. Lazar, J. Piecha, A. Bussmann-Holder, J. H. Ko and K. Roleder, *J. Alloys Compd.*, 2020, **812**, 152090.
- 16 H. Liu, L. Fan, S. Sun, K. Lin, Y. Ren, X. Tan, X. Xing and J. Chen, *Acta Mater.*, 2020, **184**, 41–49.
- 17 X.-K. Wei, C.-L. Jia, H.-C. Du, K. Roleder, J. Mayer and R. E. Dunin-Borkowski, *Adv. Mater.*, 2020, **32**, 1907208.
- 18 G. Shirane, E. Sawaguchi and Y. Takagi, *Phys. Rev.*, 1951, **84**, 476.
- 19 B. Scott and G. Burns, *J. Am. Ceram. Soc.*, 1972, **55**, 331–333.
- 20 V. J. Tennery, *J. Am. Ceram. Soc.*, 1966, **49**, 483–486.
- 21 L. Benguigui, *J. Solid State Chem.*, 1971, **3**, 381–386.
- 22 H. Wang, Y. Liu, T. Yang and S. Zhang, *Adv. Funct. Mater.*, 2019, **29**, 1807321.
- 23 X. Liu, Y. Zhao, N. Sun, Y. Li and X. Hao, *Chem. Eng. J.*, 2021, **417**, 128032.
- 24 X.-K. Wei, R. E. Dunin-Borkowski and J. Mayer, *Materials*, 2021, **14**, 7854.
- 25 Z. An, H. Yokota, N. Zhang, M. Pasciak, J. Fabry, M. Kopecky, J. Kub, G. Zhang, A. M. Glazer, T. R. Welberry, W. Ren and Z.-G. Ye, *Phys. Rev. B*, 2021, **103**, 054113.
- 26 Z. Liu, Y. Yuan, Z. Luo, H. Wan, P. Gao, H. Wu, J. Zhuang, J. Zhang, N. Zhang, H. Liu, W. Ren and Z.-G. Ye, *J. Mater. Chem. C*, 2020, **8**, 5795–5806.
- 27 F. Li, W. Liu, X. Lou, J. Zhai and C. Wang, *Appl. Phys. Lett.*, 2022, **120**, 023902.
- 28 Z. Fu, X. Chen, Z. Li, T. Hu, L. Zhang, P. Lu, S. Zhang, G. Wang, X. Dong and F. Xu, *Nat. Commun.*, 2020, **11**, 3809.
- 29 K. Roleder and J. Dee, *J. Phys.: Condens. Matter*, 1989, **1**, 1503.
- 30 P. Gao, C. Liu, Z. Liu, H. Wan, Y. Yuan, H. Li, Y. Pu and Z.-G. Ye, *J. Eur. Ceram. Soc.*, 2022, **42**, 1370–1379.
- 31 X. Yang, F. Zhuo, Z. Wang, L. Lv, Y. Liu, C. He and X. Long, *ACS Appl. Mater. Interfaces*, 2020, **12**, 28239–28245.
- 32 F. Zhuo, Q. Li, J. Gao, Q. Yan, Y. Zhang, X. Xi and X. Chu, *Phys. Chem. Chem. Phys.*, 2017, **19**, 13534–13546.
- 33 A. A. Belik, *J. Solid State Chem.*, 2012, **195**, 32–40.
- 34 Z. Liu, H. Wu, W. Ren and Z.-G. Ye, *Acta Mater.*, 2018, **149**, 132–141.
- 35 Z. Liu, H. Wu, J. Zhuang, G. Niu, N. Zhang, W. Ren and Z.-G. Ye, *CrystEngComm*, 2022, **24**, 220–230.
- 36 Y. H. Bing and Z. G. Ye, *J. Cryst. Growth*, 2006, **287**, 326–329.
- 37 K. Song, Z. Li, H. Guo, Z. Xu and S. Fan, *J. Appl. Phys.*, 2018, **123**, 154107.
- 38 R. Shannon, *Acta Crystallogr., Sect. A: Cryst. Phys., Diffr., Theor. Gen. Crystallogr.*, 1976, **32**, 751–767.
- 39 F. Jona, G. Shirane, F. Mazzi and R. Pepinsky, *Phys. Rev.*, 1957, **105**, 849.
- 40 B. Fan, F. Liu, G. Yang, H. Li, G. Zhang, S. Jiang and Q. Wang, *IET Nanodielect.*, 2018, **1**, 32–40.
- 41 Q. Li, F.-Z. Yao, Y. Liu, G. Zhang, H. Wang and Q. Wang, *Ann. Rev. Mater. Res.*, 2018, **48**, 219–243.
- 42 Z.-G. Ye and M. Dong, *J. Appl. Phys.*, 2000, **87**, 2312–2319.
- 43 C. T. Nelson, P. Gao, J. R. Jokisaari, C. Heikes, C. Adamo, A. Melville, S.-H. Baek, C. M. Folkman, B. Winchester, Y. Gu, Y. Liu, K. Zhang, E. Wang, J. Li, L.-Q. Chen, C.-B. Eom, D. G. Schlom and X. Pan, *Science*, 2011, **334**, 968–971.
- 44 Z. Chen, L. Hong, F. Wang, S. P. Ringer, L.-Q. Chen, H. Luo and X. Liao, *Phys. Rev. Lett.*, 2017, **118**, 017601.
- 45 H. J. Lee, T. Shimizu, H. Funakubo, Y. Imai, O. Sakata, S. H. Hwang, T. Y. Kim, C. Yoon, C. Dai, L. Q. Chen, S. Y. Lee and J. Y. Jo, *Phys. Rev. Lett.*, 2019, **123**, 217601.
- 46 G. Yuan, H. Huang, C. Li, D. Liu, Z. Cheng and D. Wu, *Adv. Electron. Mater.*, 2020, **6**, 2000300.
- 47 F. Li, S. Zhang, Z. Xu and L.-Q. Chen, *Adv. Funct. Mater.*, 2017, **27**, 1700310.
- 48 A. K. Tagantsev, L. E. Cross and J. Fousek, *Domains in Ferroic Crystals and Thin Films*, Springer, New York, 2010.
- 49 A. Bussmann-Holder, H. Beige and G. Völkel, *Phys. Rev. B: Condens. Matter Mater. Phys.*, 2009, **79**, 184111.
- 50 A. Bussmann-Holder, J. H. Ko, A. Majchrowski, M. Górný and K. Roleder, *J. Phys.: Condens. Matter*, 2013, **25**, 212202.
- 51 G. Arlt, *J. Mater. Sci.*, 1990, **25**, 2655–2666.
- 52 Y. Li, Q. Li, Q. Yan, Y. Zhang, X. Xi, X. Chu and W. Cao, *Appl. Phys. Lett.*, 2012, **101**, 132904.
- 53 W. Cao and G. R. Barsch, *Phys. Rev. B: Condens. Matter Mater. Phys.*, 1990, **41**, 4334–4348.
- 54 J. Hlinka, T. Ostapchuk, E. Buixaderas, C. Kadlec, P. Kuzel, I. Gregora, J. Kroupa, M. Savinov, A. Klic and J. Drahokoupil, *Phys. Rev. Lett.*, 2014, **112**, 197601.